A novel method for the optimization of positron emission tomography scanners imaging performance

Christos M. Michail[1] PhD, George. E. Karpetas[2] PhD, George P. Fountos[1] PhD, Nektarios I. Kalyvas[1] PhD, Ioannis G. Valais[1] PhD, Christina Fountzoula[3] PhD, Antonis Zanglis[4] MD, PhD, Ioannis S. Kandarakis[1] PhD, George S. Panayiotakis[2] PhD

1. Technological Educational Institute (TEI) of Athens, Department of Biomedical Engineering, Ag. Spyridonos, 12210, Athens, Greece
2.Department of Medical Physics, Faculty of Medicine, University of Patras, 265 00 Patras, Greece
3.Technological Educational Institute of Athens, Department of Medical Laboratories, Faculty of Health and Caring Profession, Ag. Spyridonos, 12210, Athens, Greece
4.Department of Nuclear Medicine, "Agios Savvas" Cancer Hospital, Athens, Greece

Keywords: -^{18}F-FDG
- Positron emission tomography
- Image quality
- Monte Carlo Geant4 for tomographic emission model
-Software for tomo-image reconstruction
-Detective quantum efficiency
-Single photon emission tomography

Corresponding author:
Assoc. Prof. Dr. G. Fountos
Department of Biomedical Engineering, Technological Educational Institution of Athens, Ag. Spyridonos Street, Egaleo, 122 10 Athens, Greece.
gfoun@teiath.gr

Received:
25 September 2016
Accepted revised:
25 October 2016

Abstract

Objective: The aim of the present study was to propose a comprehensive method for positron emission tomography (PET) scanners image quality assessment, by simulation of a thin layer chromatography (TLC) flood source with a previously validated Monte Carlo model. **Materials and Methods:** We used the GATE Monte Carlo package (GEANT4 application for tomographic emission) and the reconstructed images were obtained using the software for tomographic image reconstruction (STIR), with cluster computing. The PET scanner used in this simulation study was the General Electric Discovery-ST (USA). The plane source that was used for the image quality assessment was a TLC plate, consisting of an aluminum (Al) foil, coated with a thin layer of silica and immersed in fluorodeoxyglucose (^{18}F-FDG) bath solution (1 MBq). The influence of different scintillating crystals on PET scanner's image quality, in terms of the modulation transfer function (MTF), the normalized noise power spectrum (NNPS) and the detective quantum efficiency (DQE), were also investigated. Modulation transfer function was estimated from transverse slices of the plane source, whereas the NNPS from the corresponding coronal slices. Images were reconstructed by the commonly used 2D filtered back projection (FBP2D), the Kinahan and Rogers FPB3-DRP and the maximum likelihood estimation (MLE)-OSMAPOSL algorithms. Images obtained using the OSMAPOSL algorithm was assessed by using 15 subsets and 3 iterations. **Results:** The PET scanner confi-guration, equipped with LuAP crystals, exhibited the optimum MTF values in both 2D and 3D FBP image reconstruction, whereas the corresponding configuration with BGO crystals exhibited the optimum MTF values after the iterative algorithm. The scanner equipped with the BGO crystals was also found to exhibit overall the lowest noise levels and the highest DQE values after algorithms. These finding indicate that the GE Discovery ST PET scanner exhibits the optimum image quality parameters, in terms of MTF, NNPS and DQE, with BGO scintillating crystals. **Conclusion:** Our new method showed that the imaging performance of PET scanners can be fully characterized and further improved by investigation of the imaging chain compo-nents through Monte Carlo methods. To this aim, a TLC based plane source was used during the simulation, in order to assess the impact of the scintillating crystal material on PET image quality, with the application of a previously validated Monte Carlo model. The aforementioned plane source can be also useful for the further development of PET and SPET scanners through GATE simulations, for clinical applications.

Hell J Nucl Med 2016; 19(3): 231-240 *Epub ahead of print: 8 November 2016* *Published online: 10 December 2016*

Introduction

Combined positron emission tomography and computed tomography (PET/CT) scanners have been an essential imaging modality for various medicine disciplines in which the in vivo radiotracer distribution is reconstructed to form a quantitative image [1]. Nowadays, there is a tremendous progress in nuclear medicine PET applications, such as the introduction of quantum dot nanocrystal particles that can be prepared and tagged with various imaging agents, or different targeting ligands for applications in diagnostics, therapeutics, theranostics and regenerative medicine [2]. The use of nanocrystals could improve intrinsic and extrinsic resolution, as well as providing higher accuracy in multimodality imaging [2].

Image performance of PET/CT scanners is affected by many factors, including photon non-co linearity, oblique detector penetration, detector size and response, positron range, photon scatter, and patient motion, all of which contribute to the decreased PET resolution and image degradation [2,3]. Thus, knowledge of their impact on the overall scanner performance, by using a single imaging performance metric would be of interest.

Detective quantum efficiency (DQE) is one of the fundamental physical variables related to image quality in radiography and refers to the efficiency of a detector in converting incident radiation into an image signal. Detective quantum efficiency is acce-

pted as the best single objective indicator of overall image quality for comparison between various imaging detector technologies [4]. Detective quantum efficiency combines spatial resolution through the modulation transfer function (MTF) and image noise through the normalized noise power spectrum (NNPS), to provide a measure of the signal to noise ratio (SNR) transfer through the imaging system, from its input to its output, as a function of spatial frequency [4]. The higher the DQE is, the better the low contrast discrimination.

Several studies have been carried out concerning PET image quality. However, in the majority of them, resolution was assessed from point sources in terms of the point spread function (PSF) and consequently from the full width at half maximum (FWHM) [5-8]. The resolution was assessed in terms of the MTF calculated from the PSF method only in a few studies [9], [10], as well as in combined micro PET/CT scanners, in which MTF was estimated in the CT detector of the combined system [11]. MTF can be also assessed from a line source through the estimation of the Line Spread Function (LSF). The use of LSF method for determining the MTF in tomographic imagers was initially introduced by Boone [12], who applied this method for CT scanners evaluation. Fountos *et al*. [13] recently introduced a similar method for Single Photon Emission Computed Tomography (SPET) scanners, by immersing an Agfa MammoRay HDR Medical X-ray film in a solution of Dithiothreitol (DTT)/Tc-99m(III)-DMSA, to obtain the MTF through the LSF method. In a previous study of our group this method, for the MTF determination, was also translated for PET [14].

The concept of DQE was previously approached by various methods in PET. According to our knowledge the overall imaging quality performance has never been assessed in terms of the spatial frequency dependent DQE for PET.

The aim of this study is to extend a previous validated Monte Carlo method for the complete characterization and the further improvement of the image quality in PET scanners [15]. This novel image quality method was tested by investigating the effect of crystal material on PET scanner performance. Scintillating crystals are crucial for the efficiency of the scanner to detect annihilation photons, the subsequent light production and propagation, in order to obtain the final PET image.

To this aim, the image quality parameters (MTF, NNPS and DQE) were estimated by the simulation using a Thin Layer Chromatography (TLC) plane source covered with ^{18}F-FDG with GATE (Geant4 Application for Tomographic Emission) Monte Carlo package [15]. The GATE package, that was developed by the Open-GATE collaboration, is an open-source extension of the Geant4 (GEometry ANd Tracking) Monte Carlo toolkit [16-18]. GATE was used in combination with the software for tomographic image reconstruction (STIR) [19] to obtain reconstructed images of the plane TLC source.

GATE offers the opportunity for more realistic dynamic biodistribution of the tracers, such as respiratory and cardiac motions, displacement of the scanner, rotation of the camera heads in SPET, tracer kinetics, time-of-flight (TOF) PET, radioactive decay and dead time effects. Furthermore, with GATE can be studied the biodistribution of radiotracers using imaging to predict the dose distribution of a therapeutic agent, or modeling the radiotracer heterogeneity within tumors in PET imaging. For example, dosimetry of Zevalin® (ibritumomab tiuxetan) labeled with yttrium-90, using GATE SPET imaging can be performed as Zevalin® labeled with indium-111 [20].

Various GATE studies have been published on implementing STIR reconstruction for PET scanners [3,15,21-23]. None of these, however, simulated the General Electric Discovery-ST (US) scanner in order to fully characterise the image quality of PET in terms of DQE.

Furthermore, the influence of the replacement of the Bismuth Germinate Oxide (BGO) crystals by other crystal materials on the image quality of the GE Discovery ST scanner was also investigated. The simulation of the plane source phantom on the GE Discovery ST PET scanner provides an accurate model that is useful to fully characterize the performance of nuclear medicine imaging systems.

Materials and Methods

Geometry of the modeled PET scanner

The scanner modeled in this study was the Discovery ST (US) PET/CT, which is an integrated PET/CT system designed for oncology imaging, both for diagnosis and for treatment planning. It was designed as a second-generation PET/CT system after evaluating PET/CT applications in thousands of patients using the GE Discovery LS, the first commercially available PET/CT system. The system incorporates BGO [24, 25] crystals with dimensions of 6.3x6.3x30 mm in the tangential, axial and radial directions, respectively [15]. The crystals were assembled into blocks of 6x6 crystals. Each block was coupled to a Photomultiplier Tube (PMT) consisting of four square channels, and is assembled in modules consisting of 8 blocks (2x4) each. The detector ring is finally comprised of 35 modules, i.e. 280 crystal blocks, or 24 rings of 420 crystals (for a total of 10080 BGO crystals). The dimensions of the rings are 88.6 cm diameter with a 15.7 cm axial and 70cm transaxial fields of view (FOV) [15].

The scanner is designed to acquire images in both 2D and 3D modes. While in 2D mode, collimation between image slices is achieved with retractable Tungsten septa (54 mm length and 0.8 mm thick) which reduce scatter by restricting the directions of gamma rays entering the crystals, i.e. only photons traveling nearly perpendicularly to the axial direction are able to enter the BGO crystal without being stopped by the septa (every image plane counts events from ±5 crystal rings). In 3D mode, the septa were absent and the system allowed oblique lines of response with all the 24 rings. The energy window width in both cases was set from 375 to 650 keV [15]. The system was also simulated by replacing the BGO crystal arrays with Yttrium Orthoaluminate Perovskite ($YAlO_3$:Ce or YAP) [24,25], Lutetium Orthoaluminate Perovskite $LuAlO_3$:Ce or LuAP:Ce, Lutetium Yttrium Orthoaluminate Perovskite ((LuY)AlO_3:Ce or LuYAP:Ce) with 70% Lutetium (Lu) atomic fraction, LuYAP:Ce with 80% Lu atomic

Table 1. *Scintillating crystals properties*

Scintillating crystal	Density (g/cm^3)	Mass Attenuation Coefficients (μ/ρ) @ 511 keV	Quantum Detection Efficiency (QDE) @ 511 keV	Decay time (ns)
BGO[a]	7.13	0.1350	0.94	300
Gd_2SiO_5:Ce[a]	6.71	0.1048	0.88	60
Lu_2SiO_5:Ce[a]	7.40	0.1174	0.93	40
LuAP:Ce[a]	8.34	0.1145	0.94	18
LuYAP:Ce-70%[a,b]	7.2	0.1080	0.90	17
LuYAP:Ce-80%[a,b,c]	7.7	0.1103	0.91	20.5
$YAlO_3$:Ced	5.37	0.0852	0.75	30

[a]*Reference 25.* [b]*Reference 36.* [c]*Reference 37.* [d]*Reference 26.*

fraction [25,27], Lutetium Oxyorthosilicate (Lu_2SiO_5:Ce or LSO) [25,28-30], and Gadolinium Oxyorthosilicate (Gd_2SiO_5: Ce or GSO) [24,25,31] crystals with dimensions equal to those of BGO (6.3x6.3x30 mm) in the tangential, axial and radial directions, respectively.

Physics processes, signal and coincidence processing

The production of secondary photons and electrons, (X-rays and δ-rays, was set to 1 GeV with an electron range up to 30 cm) [18] similarly with Geant4 [16]. The calculated Quantum Detection Efficiency (QDE) [32,33] and Mass Attenuation Coefficients [34] *(μ/ρ)* of the 3 cm long crystals, under investigation, are listed in Table 1. The sinogram output file (.ima), obtained from the emission computerized axial tomography (ECAT) system, which is a raw data file (unsigned short integer), were used by STIR as input file for the reconstruction of the simulated plane source image [35]. All simulations were performed using a computer cluster with 12 dual core Intel(R) Xeon(TM) CPU 3.00GHz processors (Supermicro SuperServer 6015B-UR/NTR, UK).

Preparation of the MTF test object

The plane source that is simulated in this study follows the works of Boone (2001) [12] for CT and Fountos et al. (2012) [13] for SPET systems. It is based on the excellent binding of ^{18}F-FDG onto TLC plates [15]. The TLC plate used was an Al foil coated with a thin layer of Silica (Al density 2.7 g/cm^3) [15]. The dimensions of the TLC plate were 5x10 cm and it was immersed in ^{18}F-FDG bath solution (1 MBq). The MTF test object (plane source, i.e. the radioactive plate) was simulated within a phantom, consisting of two semi-cylindrical polyethylene blocks with 20 cm diameter and 70 cm length, in the horizontal and vertical direction for both 2D and 3D data acquisitions [15]. Plane source images were acquired from STIR, after reconstruction of the arc corrected sinogram data, with the commonly used 2D filtered back projection (FBP2D) (ramp filter 0.5) [38], the Kinahan and Rogers (2012, 1989) [38,39] FPB3DRP [38] (Colsher filter 0.5) [40] and the maximum likelihood estimation (MLE)-OSMA-POSL [38] algorithms.

Modulation transfer function (MTF)

Image quality was assessed in terms of the MTF that was obtained, by using the LSF method. In the LSF method, the thin plane source was simulated at a slight angle of 3° with respect to the horizontal or vertical axis. This technique was followed in order to avoid aliasing effects, as described in the Fujita technique [12,13,41]. Considering angles greater than 8°, the dimensions of the vertical LSFs will be different from those of the true LSFs by more than 1% and geometrical corrections should then be applied [12]. The final LSF was obtained by averaging all line LSF profiles after angle correction. The angle correction was performed following the procedure described by Fountos et al. [13]. The line LSF profile can be written as LSF(x)=G(i_x,i_y), where G(i_x,i_y) represents the slit region of interest (ROI) image pixel values. i_x, i_y are the pixel coordinates in the horizontal and vertical axes respectively, ranging as follows $x_1 \leqslant i_x \leqslant x_2$, $y_1 \leqslant i_y \leqslant y_2$ [41]. x_1, x_2 define the range, where each line LSF was calculated and y_1, y_2 are the corresponding lengths. The average LSF profile was calculated as [41]:

$$LSF(\xi) = \frac{\sum_{i_x=x_1}^{x_2} i_x \sum_{i_y=y_1}^{y_2} i_y G(i_x, i_y)}{\sum_{i_x=x_1}^{x_2} i_x \sum_{i_y=y_1}^{y_2} i_y 1} \quad (1)$$

where ξ=tan (θ)·x_i+y_i and θ is the angle between the line image and the horizontal or vertical axis. Since the plane source could have been positioned either clockwise or counter clockwise, in a slight angle ranging from -8° to -2°and 2° to 8°, a custom made software was used [13,15] for angle correction. In this study the MTF of the PET scanner was esti-

mated by averaging line profiles across the whole length of the plane source transverse image. Fourier transformation and subsequent normalization were then applied on the final LSF to compute the MTF [12-15].

Normalized noise power spectrum (NNPS)

To estimate noise, NNPS data were obtained at the same activity concentration as that of the MTF from the coronal images, using a standard 2D NNPS algorithm. A sub-image was first extracted from the coronal plane images. Half overlapping ROIs were then taken from the sub-images. The mean pixel value from each ROI was calculated and subtracted from each ROI. Thus an image corresponding to signal variations remained. The squared modulus of the 2D fast fourier transform (FFT) of each ROI was calculated and added to the NPS ensemble. This was repeated for all the ROIs taken from each image. Finally, the NNPS was calculated by dividing with the square mean value of the sub-image and afterwards the ensemble average was obtained according to (2) [42,43]:

$$NPS(v,u) = \lim_{X,Y\to\infty}\left\langle \frac{1}{XY}\left|\int_{-X/2}^{X/2}\int_{-Y/2}^{Y/2} p(x,y)\times e^{-2\pi i(vx+uy)}dxdy\right|^{2}\right\rangle \quad (2)$$

where the terms inside the brackets < > stand for ensemble average. *p(x,y)* is the difference between the average image signal and the signal at points x, y of the spatial coordinates, sampled at regular intervals *(dx,dy)*.

Detective quantum efficiency (DQE)

Detective Quantum Efficiency (DQE) is one of the fundamental physical variables related to image quality in imaging systems and refers to the efficiency of a detector in converting an incident signal into an image signal. DQE is calculated by comparing the signal-to-noise ratio at the detector output with that at the detector input as a function of spatial frequency $DQE = SNR^2_{out}/SNR^2_{in}$ [44]. According to this, SNR_{out} and SNR_{in} are the output and input signal to noise ratios respectively. DQE is dependent on radiation exposure, spatial frequency, MTF, NNPS and detector material.

High DQE values indicate that less radiation is needed to achieve identical image quality; increasing the DQE and leaving radiation exposure constant will improve image quality [45].

The ideal detector should have a DQE of 1, meaning that all the radiation energy is absorbed and converted into image information. During the past few years, various methods of measuring DQE have been established, making the comparison of DQE values difficult if not impossible as described previously (see introduction section). The DQE of the PET scanner was calculated from the MTF, NNPS, and incoming SNR^2_{in} as described in previous publications by using (3) [44]:

$$DQE(u) = \frac{MTF^{2}(u)}{SNR_{in}^{2}\cdot NNPS(u)} \quad (3)$$

Finally, DQE was calculated with incoming SNR^2_{in} defined as the plane source phantom activity (counts/mm2) incident on the detectors. Since the spatial frequency sampling steps of MTF and NNPS are generally not the same, NNPS was linearly interpolated at the frequency sampling points of MTF and then DQE was calculated at these points.

Results and Discussion

Image reconstruction

Figure 1 shows transverse and coronal slices (tilted by 3°), from the horizontal plane source images with the FBP2D, FBP3DRP and OSMAPOSL algorithms. The first column, in Figure1, shows the crystal scintillator material, the second the transverse slices of the FBP2D, the third the transverse slices of the FBP3DRP and the fourth the transverse slices of the OSMAPOSL algorithms, which were used for the MTF calculation, respectively [13]. Accordingly, the second column, in Figure 1, shows the coronal slices of the FBP2D, the third the coronal slices of the FBP3DRP and the last the coronal slices of the OSMAPOSL algorithms, which were used for the NNPS calculation, respectively. The impact on image quality of the detector material is initially depicted by inspection of Figure 1.

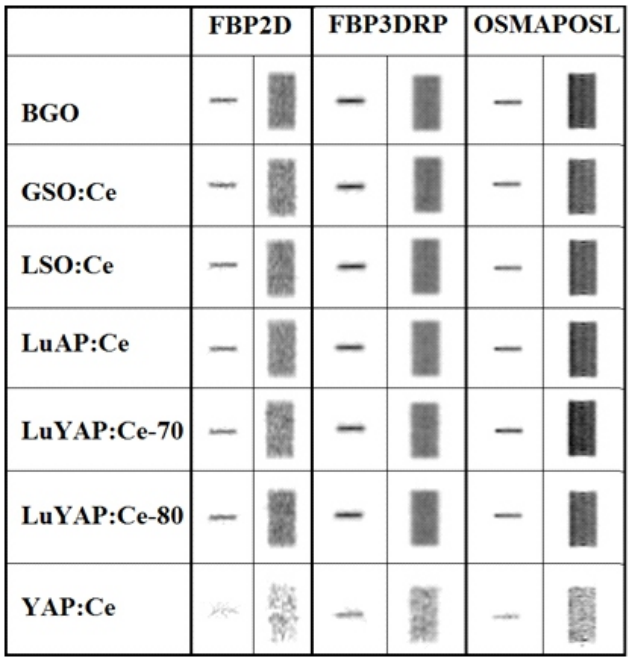

Figure 1. Transverse and coronal slices of the plane source images with the FBP2D, FBP3DRP and OSMAPOSL algorithms.

MTF

Figures 2 to 4 show comparisons between the MTF curves obtained from the horizontal plane source images, with the FBP2D, FBP3DRP and OSMAPOSL algorithms for the PET scanner configurations incorporating successively BGO, YAP, LuAP, LuYAP-70, LuYAP-80, LSO and GSO crystals. The PET scanner configuration incorporating LuAP crystals provided the optimum MTFs in both 2D and 3D FBP image reconstru-

ction whereas the configuration with BGO was found with the higher MTF values after the iterative algorithm.

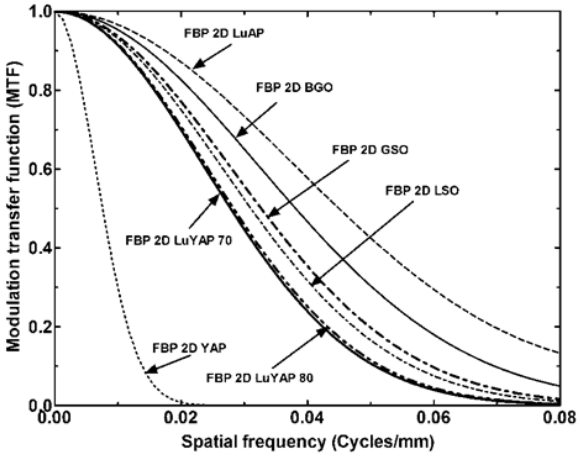

Figure 2. Comparison between the MTFs obtained from the plane source reconstructed images with the FBP2D for various crystals.

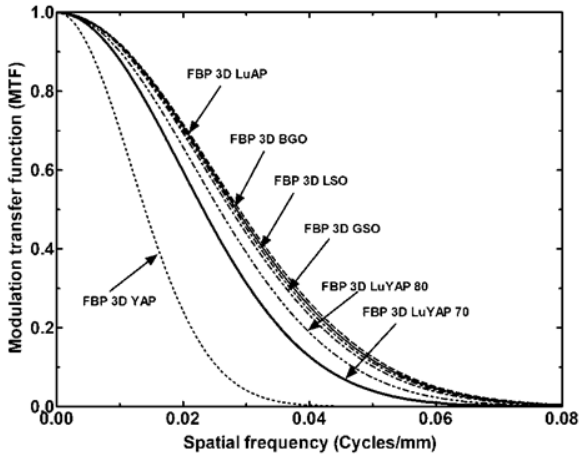

Figure 3. Comparison between the MTFs obtained from the plane source reconstructed images with the FBP3DRP for various crystals.

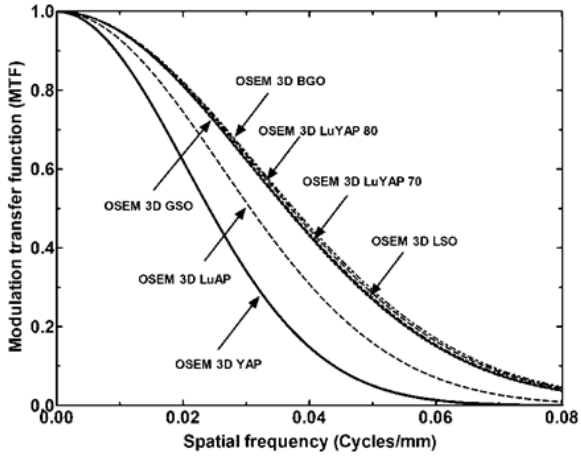

Figure 4. Comparison between the MTFs obtained from the plane source images with the OSMAPOSL (15 subsets, 3 iterations) for various crystals.

Figure 5 shows a comparison between MTF values of this work simulated with GATE and experimental MTF data in 3D mode for the GE Discovery ST PET/CT scanner [46]. Deviations are less than 10.2% which is the percentage difference value at 0.05 cycles/mm.

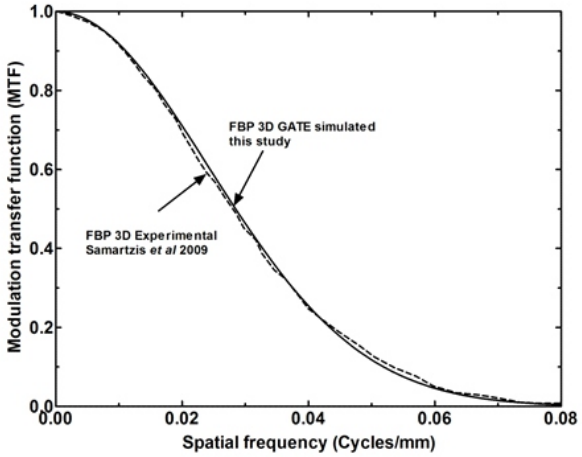

Figure 5. Comparison between the simulated and experimental MTF data in 3D mode for the GE Discovery ST PET/CT scanner.

NNPS

Figures 6 to 8 show NNPS results from the coronal slices, obtained from the FBP2D, FBP3DRP and OSMAPOSL algorithms, for the PET scanner configurations incorporating BGO, YAP, LuAP, LuYAP-70, LuYAP-80, LSO and GSO crystals. The configuration with the lowest noise levels was that incorporating BGO crystals. This finding, along with the data provided in Table 1, verifies the validity for the commercial use of BGO crystals choice in the assembly of the particular PET system.

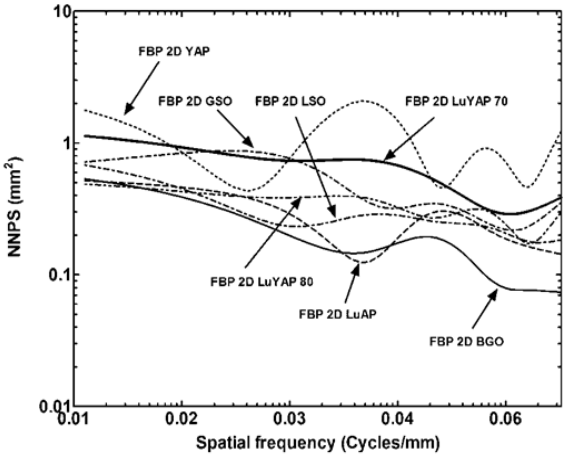

Figure 6. Comparison between the NNPS obtained from the plane source reconstructed images with the FBP2D for various crystals.

DQE

Table 2 shows the calculated true coincidences counted by all the crystal/detector electronics combinations under investigation. Figures 9 to 11 show DQE results obtained from

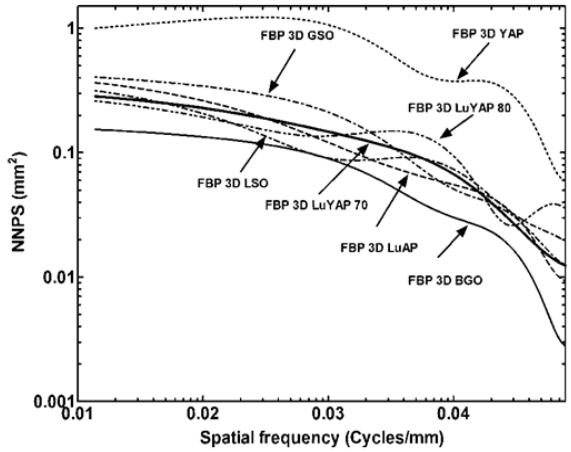

Figure 7. Comparison between the NNPS obtained from the plane source reconstructed images with the FBP3DRP for various crystals.

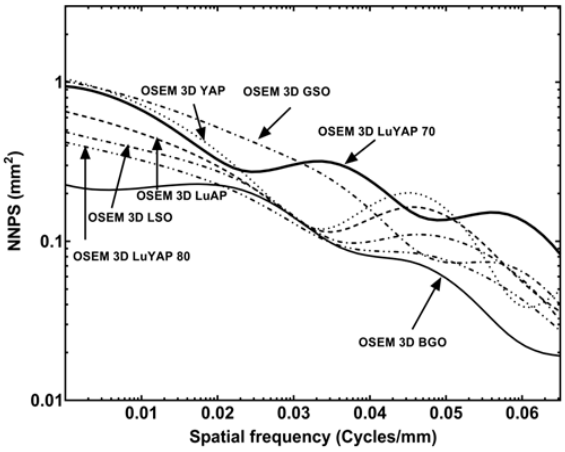

Figure 8. Comparison between the NNPS obtained from the plane source images with the OSMAPOSL (15 subsets, 3 iterations) for various crystals.

the FBP2D, FBP3DRP and OSMAPOSL algorithms, for the PET scanner configurations incorporating successively BGO, YAP, LuAP, LuYAP-70, LuYAP-80, LSO and GSO crystals. The curves correspond to the combined MTF and NNPS results from both the transverse and coronal slices. The behavior of the DQE was influenced by both MTF and NNPS. DQE values of the PET configuration incorporating BGO crystals were found higher after FBP3DRP and OSMAPOSL algorithms examined in this study. DQE values of the LuYAP were found higher after FBP2D.

In Figures 9 to 11 the DQE results provided the overall performance of a PET scanner. However these results cannot be straightforward translated into predictions about the clini-cal usefulness of images produced by the system for a hu-man observer [47]. When the quantum noise is a limiting fac-tor for the observer, the performance is dependent on the task, and hence the relevance of the DQE at different spatial frequencies varies. Due to this, cumulative image quality results, in the sense of Figures of Merit (FOMs), were also obtained by integrating the entire MTF, NNPS and DQE (all spatial frequencies were given equal weight). The single index values obtained this way are related to the performance of the ideal observer in the task of detecting a point source. However, for any other task, a different weighting of the frequencies must be used and, consequently, the optimal system setting for obtaining the maximal FOM will change [47].

Table 2. *Calculated true coincidences counted by all the crystal/detector electronics*

Scintillating crystal	True counts/mm^2
BGO	108.27
Gd_2SiO_5:Ce	50.04
Lu_2SiO_5:Ce	82.13
LuAP:Ce	85.13
LuYAP:Ce-70%	57.43
LuYAP:Ce-80%)	66.93
$YAlO_3$:Ce	2.88

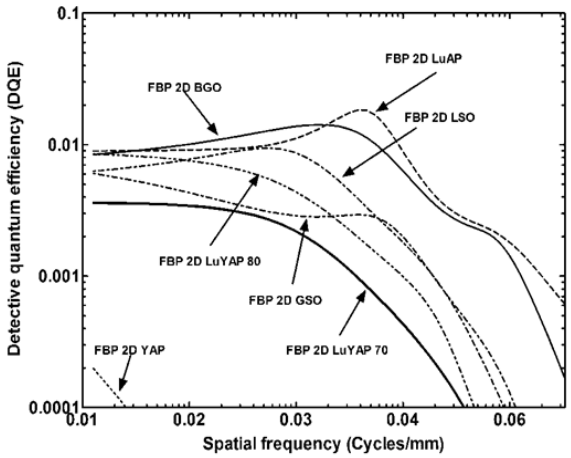

Figure 9. Comparison between the DQEs obtained from the plane source reconstructed images with the FBP2D for various crystals.

Table 3 shows these results for all the crystals in the spatial frequency range under investigation. As it can be depicted from this Table the Discovery ST PET scanner provided the optimum image quality combined with BGO scintillating crystals. This can be also explained by taking also into consideration the mass attenuation coefficient (μ/ρ= 0.13-50) value and the quantum detection efficiency (QDE= 0.94) at 511 keV which is the highest among the crystals under investigation.

The influence of the crystal material and the different image reconstruction algorithms can be also depicted on complex human structures as shown in Figure 12, where the grey scales have been translated to activity distributions.

Table 3. *Imaging performance comparison between the various scintillating crystals.*

Scintillating detectors	Imaging Performance								
	MTF			NNPS			DQE		
	Reconstruction algorithm								
	2D FBP	FBP3D RP	3D OSEM	2D FBP	FBP3D RP	3D OSEM	2D FBP	FBP3D RP	3D OSEM
BGO	31.12	43.10	34.51	15.11	6.94	7.64	0.37	1.39	0.80
GSO:Ce	26.96	41.73	33.39	29.17	17.24	21.46	0.15	0.54	0.30
LSO:Ce	25.67	42.51	33.51	22.03	13.34	11.51	0.20	0.78	0.30
LuAP:Ce	36.05	43.70	28.54	18.48	14.74	14.04	0.42	0.75	0.32
LuYAP:Ce-70	23.09	35.21	33.71	41.92	12.92	20.39	0.08	0.50	0.30
LuYAP:Ce-80	23.48	39.06	34.15	21.88	12.98	9.73	0.18	0.63	0.64
YAP:Ce	6.66	21.43	22.56	73.49	59.79	19.22	0.01	0.08	0.16

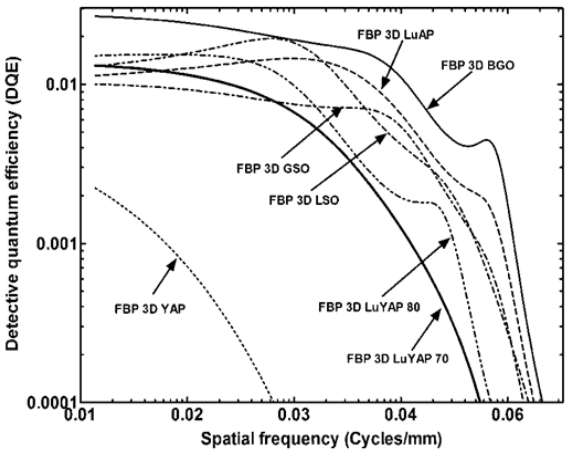

Figure 10. Comparison between the DQEs obtained from the plane source reconstructed images with the FBP3DRP for various crystals.

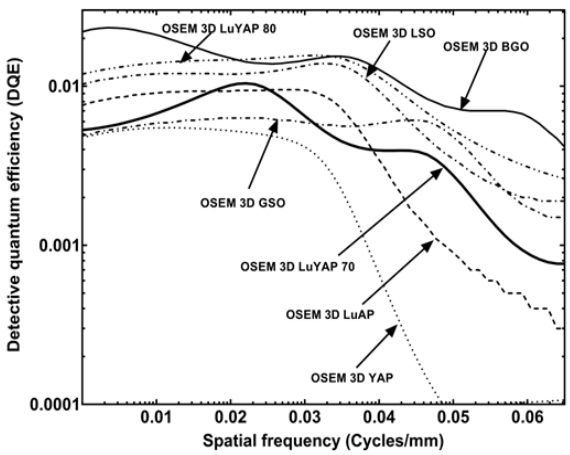

Figure 11. Comparison between the DQEs obtained from the plane source images with the OSMAPOSL (15 subsets, 3 iterations) for various crystals.

In order to obtain these slices, a brain phantom (Hoffman) [48,49] was used for the simulation. The brain slices were acquired from STIR, after reconstruction of the arc-corrected sinogram data with the commonly used 2D filtered back projection (FBP2D) (Ramp filter with additional apodizing window 0.5), the Kinahan and Rogers FPB3DRP (Colsher filter with additional apodizing window 0.5) and with the iterative, maximum likelihood estimation Ordered Subsets version of Green's MAP one step late (MLE-OSMAPOSL) algorithms [38]. The phantom acquired images, after reconstructing with various algorithms and obtained using different scintillator materials, were also visually assessed by two independent and blinded nuclear medicine physicians.

The major brain anatomic landmarks (i.e. ventricles, sulci) were used for the visual assessment. The subjective image quality was then semi-quantified using a visual scale score of 1 to 5 (5: corresponds to the best image). In all cases, the OSMAPOSL images were assessed as having the best image quality. The following scores were attributed for each image: 5 for the BGO, 2 for the Gd_2SiO_5:Ce, 3 for the Lu_2SiO_5:Ce, 3 for the LuAP:Ce, 4 for the LuYAP:Ce-70%, 4 for the LuYAP:Ce-80% and 1 for the YAlO3:Ce images.

Interpretation of results

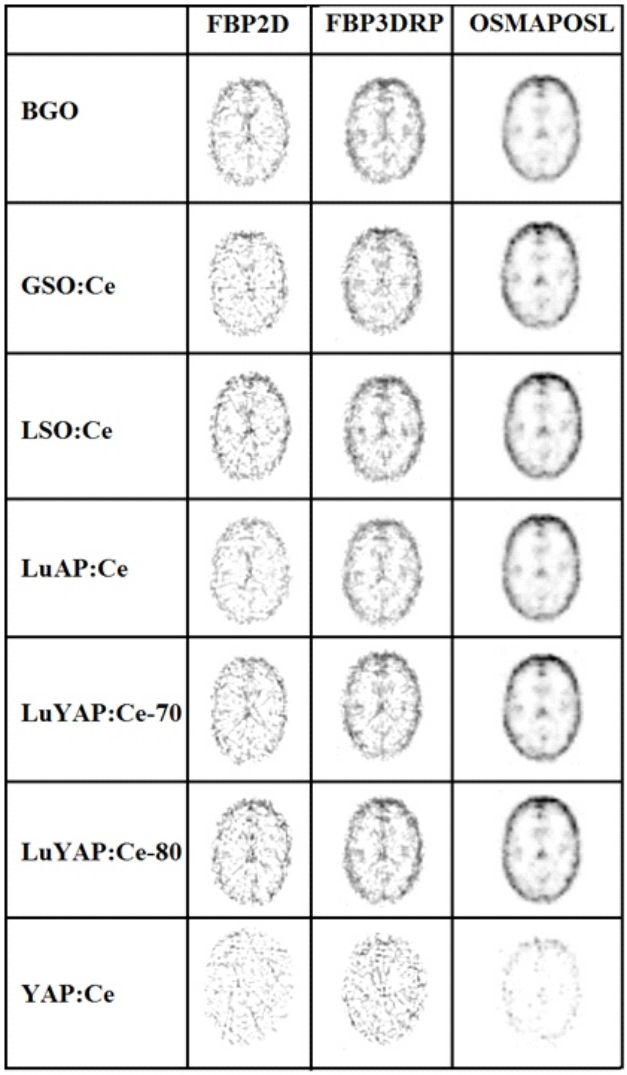

Figure 12. Hoffman brain phantom in 2D (left), 3D (middle) and OSEM with 15 subsets/3 iterations (right).

In this study a novel image quality method for PET scanners was implemented with GATE Monte Carlo methods. PET images were obtained from STIR reconstruction software through the simulation of a novel thin ^{18}F-FDG plane source. Furthermore, the STIR reconstructed GATE simulated data were used to obtain PET images from specific radiopharmaceutical distribution using simplified phantoms or more complex human structures. The above results will assist nuclear medicine physicians, as an efficient diagnostic tool. The STIR reconstructed images, could also be used to bridge the gap between imaging and dosimetry, in order to obtain directly dose maps from the activity distribution as input for PET and SPET Monte Carlo simulations [50]. From the latter, physicians could directly compare the actual dose biodistribution map of a tracer, used for the production of SPET or PET data, with the data estimated from the reconstructed PET or SPET images.

Image quality was assessed from the reconstructed images, by the estimation of the spatial frequency dependent MTF, NNPS and DQE of the plane source reconstructed images.

The influence of the detector material on the image quality of a PET scanner was also investigated. Our study showed that: a) Lu-AP crystal provided the optimum MTFs in both 2D and 3D FBP image reconstruction whereas BGO was found with the higher MTF values after the iterative algorithm, b) BGO crystals were also found with the lowest noise levels and the highest DQE values after all image reconstruction algorithms (except from the 2D DQE values where LuYAP was found with the highest values). These finding show that the BGO crystal provided the optimum overall image quality parameters for the specific PET scanner implementation, however the rather slow decay time of this material is a drawback for time of flight applications [51,52].

In conclusion, in this study the method modelled and simulated can be experimentally implemented and used for the routine PET quality control. In this study was used for the image quality assessment and optimisation, but it can be also useful for the further development of PET and SPECT scanners though GATE simulations.

Acknowledgment

Authors wish to thank Dr. Ross Schmidtlein for the support on GATE development. Authors wish also to thank Dr. Kris Thielemans Senior Lecturer (University College London) and Dr. Harris Tsoubas Lecturer (University of Leeds) for the helpful discussions concerning STIR reconstruction (http://stir.sourceforge.net).

Authors Christos Michail, Ioannis Valais and Christina Fountzoula wish also to thank the Special Account for Research Grants of the TEI of Athens, in the framework of the Internal Programme for the Support of the TEI of Athens Researchers, for 2015, code 80224 for the financial support of this research.

The authors declare that they have no conflicts of interest

Bibliography

1. Bushberg J, Siebert J, Leidholdt E et al. *The essential physics of medical imaging.* (Lippincott Williams & Wilkins, Philadelphia 2002), 577-749.
2. Assadi M, Afrasiabi K, Nabipour I, Seyedabadi M. Nanotechnology and nuclear medicine; research and preclinical applications. *Hell J Nucl Med* 2011; 14(2): 149-159
3. Schmidtlein C R, Kirov A S, Nehmeh S A et al. Validation of GATE Monte Carlo simulations of the GE Advance/Discovery LS PET scanners. *Med Phys* 2006; 33(1):198-208.
4. Michail C, Valais I, Martini N et al. Determination of the Detective Quantum Efficiency (DQE) of CMOS/CsI Imaging Detectors following the novel IEC 62220-1-1:2015 International Standard *Radiat Meas* 2016; 94:8-17.
5. Lartizien C, Kuntner C, Goertzen A et al. Validation of PET-SORTEO Monte Carlo simulations for the geometries of the MicroPET R4 and Focus 220 PET scanners. *Phys Med Biol* 2007; 52:4845-4862.
6. Lodge M, Rahmim A and Wahl R, A Practical, Automated Quality Assurance Method for Measuring Spatial Resolution in PET. *J Nucl Med* 2009; 50:1307-1314.
7. Bettinardi V, Presotto L, Rapisard E et al. Physical Performance of the

new hybrid PET /CT Discovery-690. *Med Phys* 2011; 38(10):5394-5411.
8. NEMA standards publication NU 2-2001: *Performance measurements of positron emission tomographs*. Technical report National Electrical Manufactures Association, Washington, DC, 2001:1-36.
9. Defrise M, Geissbuhler A and Townsend D W, A performance study of 3D reconstruction algorithms for positron emission tomography. *Phys Med Biol* 1994; 39:305-320.
10. Stickel J R and Cherry S R, High-resolution PET detector design: modelling components of intrinsic spatial resolution. *Phys Med Biol* 2005; 50:179-195.
11. Liang H, Yang Y, Yang K et al. A microPET/CT system for in vivo small animal imaging. *Phys Med Biol* 2007; 52:3881-3894.
12. Boone J M, Determination of the presampled MTF in computed tomography. *Med Phys* 2001; 28:356-360.
13. Fountos G P, Michail C M, Zanglis A et al. A novel easy-to-use phantom for the determination of MTF in SPECT scanners. *Med Phys* 2012; 39(3):1561-1570.
14. Karpetas G, Michail C, Fountos G et al. A new PET resolution measurement method through Monte Carlo simulations. *Nucl Med Com* 2014; 35(8).
15. Karpetas G E, Michail C M, Fountos G P et al. Towards the optimization of nuclear medicine procedures for better spatial resolution, sensitivity, scan image quality and quantitation measurements by using a new Monte Carlo model featuring PET imaging. *Hell J Nucl Med* 2013; 16(2):111-120.
16. Jan S, Santin G, Strul D et al. GATE: A simulation toolkit for PET and SPECT. *Phys Med Biol* 2004; 49:4543-4561.
17. Strul D, Santin G, Lazaro D et al. GATE (Geant4 application for tomographic emission): A PET/SPECT general purpose simulation platform. *Nucl Phys B* 2003; 125:75-79.
18. Agostinelli S, Allison J, Amako K et al. Geant4-a simulation toolkit. *Nucl Instrum Meth Phys Res A* 506 (2003) 250-303.
19. Thielemans K, Tsoumpas C, Mustafovic S et al. STIR: software for tomographic image reconstruction release 2. *Phys Med Biol* 2012; 57:867-883.
20. Visvikis D, Bardies M, Chiavassa S et al. Use of the GATE Monte Carlo package for dosimetry applications. *Nucl Instrum Meth A* 2006; 569: 335-40.
21. Polycarpou I, Marsden P K and Tsoumpas C. Evaluation of two approaches to motion-corrected PET image reconstruction. *J of Physics* 2011; 317:012001.
22. Ghazanfari N, Sarkar S, Loudos G, Ay MR. Quantitative assessment of crystal material and size on the performance of rotating dual head small animal PET scanners using Monte Carlo modeling. *Hell J Nucl Med* 2012; 15(1): 33-39.
23. Delso G, Martinez M J, Torres I et al. Monte Carlo simulations of the count rate performance of a clinical whole-body MR/PET scanner. *Med Phys* 2009; 36(9):4126-4135.
24. Valais I, Michail C, David S et al. A Comparative Study of the Luminescence Properties of LYSO:Ce, LSO:Ce, GSO:Ce and BGO Single Crystal Scintillators for Use in Medical X-Ray Imaging. *Physica Medica* 2008; 24:122-125.
25. Van Eijk C W E, Inorganic scintillators in medical imaging. *Phys Med Biol* 2002; 47:R85-R106.
26. Kalivas N, Valais I, Salemis G et al. Imaging properties of cerium doped Yttrium Aluminum Oxide (YAP:Ce) powder scintillating screens under X-ray excitation. *Nucl Instrum Meth Phys Res A* 569 (2006) 210-214.
27. Valais I G, Michail C M, David S L et al. Comparative Investigation of Ce^{3+} doped Scintillators in a wide Range of Photon Energies covering X-ray CT, Nuclear Medicine and Megavoltage Radiation Therapy Portal Imaging applications. *IEEE Trans Nucl Sci* 2010; 57(1):3-7.
28. Michail C, David S, Liaparinos P et al. Evaluation of the imaging performance of LSO powder scintillator for use in x-ray mammography. *Nucl Instrum Meth Phys Res A* 2007; 580:558-561.
29. Michail C M, Fountos G P, David S L et al. A comparative investigation of Lu_2SiO_5:Ce and Gd_2O_2S:Eu powder scintillators for use in x-ray mammography detectors. *Meas Sci Technol* 2009; 20:104008.
30. Michail C, Toutountzis A, David S et al. Imaging performance and light emission efficiency of Lu_2SiO_5:Ce (LSO:Ce) powder scintillator under x-ray mammographic conditions. *App Phys B* 2009; 95:131-139.
31. Valais I, David S, Michail C et al. Investigation of luminescence properties of the LSO:Ce, LYSO:Ce and GSO:Ce crystal scintillators under low-energy γ-ray excitation used in nuclear imaging. *Nucl Instrum Meth Phys Res A* 2007; 581:99-102.
32. Boone J: in *Handbook of Medical Imaging: Physics and Psychophysics,* edited by J. Beutel, H. L. Kundel, R. L. Van Metter (SPIE, Bellingham, WA, 2000), Vol. 1, pp 36-57.
33. Michail C M, Fountos G P, Liaparinos P F et al. Light emission efficiency and imaging performance of Gd_2O_2S:Eu powder scintillator under X-ray Radiography conditions. *Med Phys* 2010; 37(7): 3694-3703.
34. Hubbel J, Seltzer S. *Tables of X-ray mass attenuation coefficients and mass energy absorption coefficients 1keV to 20MeV for elements Z=1 to 92 and 48 additional substances of dosimetric interest*. U.S. Department of commerce. NISTIR 5632 (1995).
35. OpenGATE Collaboration: http://www.opengatecollaboration.org/.
36. Lecoq P, Annenkov A, Gektin A et al. Inorganic Scintillators for Detector Systems, Physical Principles and Crystal Engineering, (Springer-Verlag, Heidelberg 2006).
37. Weber S, Christ D, Kurzeja M, et al. Comparison of LuYAP, LSO, and BGO as Scintillators for High Resolution PET Detectors. *IEEE Trans. Nucl Sci* 2003; 50(5):1370-1372.
38. Thielemans K, Tsoubas C, Sauge D et al. STIR Software for Tomographic Image Reconstruction User's Guide Version 2.4: http://stir.sourceforge.net/documentation/ STIR-UsersGuide.pdf (2012) pp.1-69.
39. Kinahan P and Rogers J. Analytic 3D image reconstruction using all detected events. *IEEE Trans Nucl Sci* 1989; 36:964-968.
40. Labbe C, Zaidi H, Morel C (updated by Thielemans K, Imanet), STIR Description of the STIR implementation of FBP 3DRP Version 0.91: http://stir.sourceforge.net/documentation/STIR-FBP3DRP.pdf (2004) pp.1-10.
41. Fujita H, Tsia D, Itoh T et al. A simple method for determining the modulation transfer function in digital radiography. *IEEE Trans Med Imaging* 1992; 11:34-39.
42. Williams M B, Mangiafico P A, Simoni P U. Noise power spectra of images from digital mammography detectors. *Med Phys* 1999; 26 (7):1279-1293.
43. Dobbins III J T: in *Handbook of Medical Imaging Physics and Psychophysics*, edited by J. Beutel, H. L. Kundel, R. L. Van Metter (SPIE, Bellingham, WA, 2000), Vol. 1, pp 161-222.
44. Dainty J C and Shaw R, *Image Science* (Academic Press, London, 1974).
45. Grammaticos P and Fountos G, The physician should benefit, not harm the patient. *Hell J Nucl Med* 2006; 9(2):82-84.
46. Samartzis A, Fountos G, Kalatzis I, et al. A novel method for the MTF determination in PET/CT scanners, World Congress on Medical Physics and Biomedical Engineering, IFMBE Proceedings, Munich, Germany, 2009; 25(2):841-844.
47. Eriksson I, Starck S and Bath M, Determination of the detective quantum efficiency of gamma camera systems: a monte carlo study. *Radiat Prot Dosim* 2010; 139(1-3):219-227.
48. Hoffman E J, Cutler P D, Digby W M et al. 3-D phantom to simulate cerebral blood flow and metabolic images for PET. *IEEE Trans Nucl Sci* 1990; 37:616-620.
49. *OpenGATE Collaboration*, Users Guide V6.1: Voxelized Source and Phantom: http://www.opengatecollaboration.org.
50. Karaoglanis K, Polycarpou I, Efthimiou N, Tsoumpas C. Appropriately regularized OSEM can improve the reconstructed PET images of data with low countstatistics. *Hell J Nucl Med* 2015;18 (2):140-145.
51. Marin-Oyaga VA, Salavati A, Houshmand S et al. Feasibility and performance of an adaptive contrast-oriented FDG PET/CT quantification technique for global disease assessment of malignant pleural mesothelioma and a brief review of the literature. *Hell J Nucl Med* 2015; 18(1):11-18.

52. Zielinski A, Behrendt FF, Verburg FA, Mottagh FM, Krohn T. Phantom studies and clinical application of high resolution, image reconstruction using ^{18}F-fluoromethylcholine PET/CT for prostate cancer. *Hell J Nucl Med* 2014;17(3):194-199.

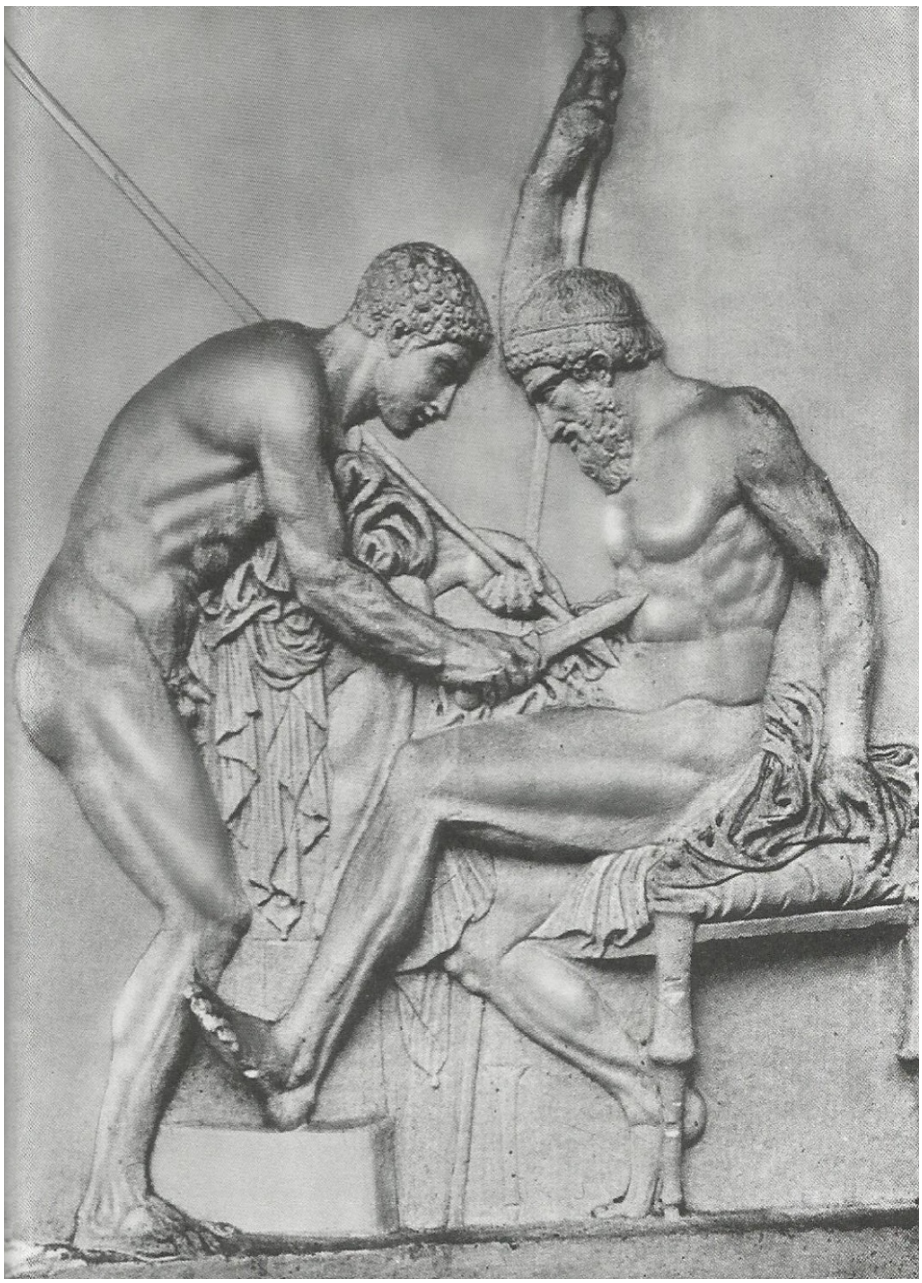

Achilles trying to heal the wound of Telephos, he himself had caused, before. Achilles is using scrapes of iron from his lance.